Verifying the relationships among the variabilities of summer precipitation extremes over western Japan in the d4PDF climate ensemble, monsoon activity, and Pacific sea surface temperature

Shao-Yi Lee[1], Sicheng He[1], Tetsuya Takemi[1]

5   [1]Disaster Prevention Research Institute, Kyoto University, Uji, Kyoto 611-0011, Japan

Correspondence to: Tetsuya Takemi (takemi@storm.dpri.kyoto-u.ac.jp)

Abstract.

Upper 99th percentile hourly and 90th percentile daily rainfall over western Japan was calculated for June–July every year, using two observation-based and one simulation-based datasets. These were 54 rain-gauges over the 1952–2022 period, 1 km
10   resolution radar/rain-gauge merged precipitation data over the 2006–2022 sub-period, and the 5 km resolution d4PDF (database for Policy Decision-making for Future climate changes) climate ensemble over the 1952–2010 sub-period. Grid-points over western Japan were clustered by applying the HDBSCAN (Hierarchical Density-Based Spatial Clustering of Applications with Noise) algorithm. Spearman correlation was calculated between rainfall extremes of the clusters, and standardised scores of four modes from the rotated extended Principle Component Analysis of Pacific SST (Sea Surface
15   Temperature) anomalies. These modes represent ENSO (El Niño-Southern Oscillation) growth, ENSO decay, warming trend, and PDV (Pacific Decadal Variability). Based on the clustering, 10 sub-regions were selected for analysis. The correlation coefficients between rainfall extremes and SST modes were at most moderate ($|R| \leqslant 0.60$) over most sub-regions, reflecting correlation with ENSO decay and warming trend, both directions with a spatial pattern for ENSO growth, and anti-correlation with PDV. These relationships could be partially explained through the strength and location of the monsoon jet
20   in relation to different ENSO phases. d4PDF reflected similar relationships for the first three modes, although it showed both spatial and strength biases. Correlation between rainfall extremes and ENSO decay was likely excessively strong in d4PDF due to the regional climate model's over-response to the monsoon jet wind speed. For the PDV mode, the model could not reproduce the observed relationship of spatially widespread anti-correlation with rainfall extremes. Based on the mostly weak long-term correlations, we concluded that individual SST modes modulated rainfall extremes but were not controlling
25   factors in their occurrence. However, we hypothesize that multiple modes may stack in ways that greatly strengthen their modulating effect, and recommend further investigation in this using sensitivity simulations on case studies.

1 Introduction

30

Extreme rainfall events in recent summers have prompted the identification of regional conditions favorable to such developments (Harada et al. 2020, Yokoyama et al. 2020, Nayak and Takemi 2021, Naka and Takemi 2023). There is concern that climate change is increasing the strength of such events (Nayak and Takemi, 2019; Kamae et al., 2021; Mori et al., 2021), and if so, there is interest in what spatio-temporal scales of rainfall are impacted (Fujibe 2016, Unuma and
35 Takemi 2021). The authors wish to evaluate the changes of monsoon rainfall extremes (if any) in the future warmer climate; for this purpose, a standard procedure of calculating climate projections begins by comparing and verifying historical or control climate simulation with observations. The possible dependence of such extremes on internal climate variability complicates the calculation of climate projections since climate variability itself may change in the future climate. Hence, in this study we evaluated the relationships between the variabilities of summer rainfall extremes over western Japan, monsoon
40 activity, and Pacific sea surface temperature (SST).

Many hemispheric-scale modes of climate variability may interact with the regional- and global-scale signals over Japan; however, since Japan is an island located at the edge of the Pacific Ocean, it seems highly possible that the modes of Pacific SST have impacts on extreme rainfall over Japan. The dominant mode of Pacific variability is the El Niño-Southern
45 Oscillation (ENSO). Although ENSO takes place in the tropical Pacific, it influences SSTs in the mid-latitudes and even globally in the form of the "Pacific-North America pattern" (Horel and Wallace 1981, Hoskins and Karoly 1981; see Alexander et al. 2002 for a literature review).

Over East Asia, the development of an El Niño during winter influences the following summer through the "Anomalous
50 Philippine Sea Anti-cyclone", persistent anti-cyclonic wind anomalies over the western North Pacific to the east of the Philippines which result in a wetter monsoon (e.g. Wang et al. 2000). The persistence of the El Niño signal has been explained by the "Indo-western Pacific Ocean Capacitor", or teleconnections into and returning from the Indian Ocean (Kosaka et al. 2013, Xie et al. 2016), which excite a series of alternating high-and-low pressure, temperature and convection across the region termed as the "Pacific-Japan" (P-J) pattern (Nitta, 1987).

55

While the El Niño-associated anomalous anti-cyclone is one lobe of the of the P-J pattern, the P-J pattern is excited not only by ENSO. A positive Indian Ocean Dipole (IOD) occurring by itself without an El Niño would also have a teleconnection to the Pacific. An extremely warm Indian Ocean since 2019 likely contributed to the extreme rainfall event of 2020 (Takaya et al. 2020), in conjunction with other exacerbating factors like the Madden-Julian Oscillation (Zhang et al. 2021). The P-J
60 pattern can also be excited by Rossby wave breaking (Takemura and Mukougawa 2022), which increases during Niña-like conditions in summer (Takemura et al. 2020). Such results suggest that it will be difficult to find clean and robust relationships between ENSO phase and rainfall over Japan.

An early study using data for a 30-year period (1951–1980) found no evident relationship between the Baiu (monsoon front)
65 rainfall and the Southern Oscillation Index (SOI) of the season (Ninomiya and Mizuno, 1987). A study using another 30-year (1963–1992) period data found that the relationship changed from Baiu rainfall lagging the Nino3 index during 1963–1977, to leading Nino3 during 1978–1992 (Tanaka, 1997). A study of rainfall in Fukuoka (in Kyushu) for about a century (1890–2000) using categorised SOI found heavy rainfall to lag the "Strong La Niña" category (Kawamura et al. 2001, Jin et al. 2005). Yet another study for 54 years (1958–2011) found that weather patterns associated with heavy rainfall over Japan
70 occurred more frequently when the Nino3.4 index of the season was high (Ohba et al. 2015). Such examples suggest that the relationship between ENSO and rainfall over Japan may depend on the period of data or even the location being studied. ENSO has a period of about 5–7 years, so even a 100-year period would contain only about 20 cycles. A 400-year study using paleoclimate proxies concluded that the strength and even sign of the relationship varied over time, and proposed that the Pacific Decadal Oscillation modulated the relationship (Sakashita et al. 2016). It appears that scientific literature is far
75 from unanimous regarding the relationship between ENSO and rainfall variability over Japan.

Since we were unable to draw satisfactory conclusions from those past studies, we decided to investigate the relationships between Pacific climate variability and extreme rainfall variability in the monsoon season over Japan in observations first,

before applying the same methodology to climate models. While long-term SST records are widely available, long-term
80   rainfall records are less so. In Japan, the number of manned weather stations with long-term rainfall records is limited. In
contrast, rainfall records with good spatial coverage, but a relatively short-term period, exist, using the combination of more
than 1000 automated weather stations and the radar network (Nagata 2011). In this study, we wish to make use of as much
data as possible, to extend the results of the above-described past studies in three ways:

85   Firstly, it is possible that the difficulty in finding a relationship with ENSO arise from heavy rainfall not being recorded.
Rain-gauges with long record periods are sparsely distributed in comparison to the spatial resolution of hourly extremes. In
contrast, radar and the automated weather station network have short record periods, but good spatial coverage. The use of
spatially dense data might reveal new information.

90   Secondly, although the SOI or Niño indices indicate the ENSO-related state of the atmosphere and ocean respectively,
ENSO phases are not instantaneous states but processes that develop and decay over the course of two years, even when
SOI/Niño indices may have similar values before and after the ENSO peak. Clearer relationships may emerge between
rainfall and an indicator measuring the direction of ENSO progress.

95   Thirdly, the value of SOI/Niño indices may reflect not only the ENSO state, but also the states of other modes, such as the
above-mentioned Pacific Decadal Oscillation. This study will directly decompose Pacific temperature anomalies through
Principle Component Analysis and correlate between each mode and extreme rainfall, instead of using the SOI/Niño indices.

The structure of this paper is organized as follows. Section 2 describes the data and methods used. Section 3 describes the
100 results from the Principle Component Analysis of Pacific SST, rainfall clustering, and correlation of SST modes with
clustered rainfall extremes. In Section 4, we attempt to explain the relationships of Section 3 in terms of monsoon activity.
Finally, Section 5 summarises the findings of the study.

2 Data and Methods

105 **2.1 Data and tools**

2.1.1 Rainfall data

The database for Policy Decision-making for Future climate changes (d4PDF) is a collection of ensemble climate simulations (Mizuta et al. 2017, Ishii and Mori 2020). A 100-member historical-warming (HPB) climate ensemble has been simulated by the Meteorological Research Institute (MRI) Atmospheric General Circulation Model (AGCM) version 3.2

110 (MRI-AGCM3.2; Mizuta et al. 2012), of which 12 members have been downscaled to hourly temporal and 5 km spatial resolutions (Kawase et al., 2023). 59-years (1952–2010) of rainfall from 10 members of the 5 km d4PDF were used for analysis. "d4PDF" in this study will refer to the downscaled rainfall; the AGCM will termed "d4PDF-AGCM".

The Automated Meteorological Data Acquisition System (AMeDAS) is network of automated surface weather stations,

115 including rain-gauges, operated by the Japan Meteorological Agency (JMA). Radar/raingauge analyzed precipitation dataset (referred to as Radar-AMeDAS) is a gridded rainfall product available from JMA, consisting of radar composites calibrated with the AMeDAS rain-gauges (Nagata 2011). A 17-year period (2006–2022) of radar-AMeDAS was used, with hourly temporal and approximately 1 km spatial resolutions. Gridded hourly rainfall was compressed by rounding to unsigned short integers, and rainfall below 1 mm hour^{-1} was set to 0 hour^{-1} mm. Rainfall at daily resolution was calculated by summing the

120 hourly values.

A 71-year period (1952–2022) dataset of hourly rain-gauge rainfall from 54 meteorological stations was obtained from JMA (https://www.data.jma.go.jp/gmd/risk/obsdl/). The station names are listed in Supp. Table S2-1. Some rain-gauges had missing data in some years. The observed cases fell into two extremes with either less than 10 days missing, or less than 10

125 days available in which case the year was removed. The years removed from each station are listed in Supp. Table S2-1.

Rainfall during June and July was analysed. This is the season when the monsoon (i.e., Baiu) front passes over the study domain of western Japan. An analysis of typhoon frequency was carried out for each month using the International Best Track Archive for Climate Stewardship (IBTrACS; Knapp et al., 2018) for observations, and Webb et al. (2019) for d4PDF.

130 The number of typhoons was found to increase substantially in August. Evaluating typhoon changes in the future climate is not trivial (e.g. Mori and Takemi, 2016 for a review), so the authors preferred to exclude typhoon-associated rainfall as much as possible, even though the typical calendar term of "summer" includes August. From a phenomenon perspective, August is climatologically quite distinct from June and July over western Japan.

135 Upper percentile rainfall will be referred to multiple times in this text. For ease of reading, these values will be referred to as Pt_{xx}, where t refers to the temporal resolution and xx to the percentile evaluated for each year. For example, Ph_{99} and Pd_{90} refer to 99th percentile hourly rainfall and to 90th percentile daily rainfall during June–July of every year, respectively.

140 **2.1.2 Sea Surface Temperature (SST)**

The historical (HPB) d4PDF-AGCM ensemble was driven by randomly perturbed SST from the Centennial Observation-Based Estimates of SST version 2 (COBE-SST2; Hirahara et al. 2014). The SST data was of 1° spatial resolution and monthly temporal resolution, and a 71-year period (1952–2022) was used for analysis. Data over the Pacific in the domain of 100°E–60°W, 20°S–60°N was used. Data on the Atlantic side was removed. Data in the domain of 135°E–160°E, 45°N–

145 60°N was also removed to exclude the Sea of Okhotsk, in order to reduce the influence of sea ice. COBE-SST (Ishii et al., 2005; Japan Meteorological Agency, 2006) was also compared with COBE-SST2, and produced similar climate modes except for the Trend mode (Supp. Material Sect. 1).

2.1.3 Other meteorological variables

150 Meteorological variables in the region of (110–150°E, 20–50°N) from d4PDF-AGCM and the Japanese 55-year Reanalysis (JRA55; Kobayashi et al., 2015) were used to evaluate the monsoon activity. The datasets were obtained at 1.25° spatial resolution. The period of 1958–2022 was used from JRA55. The period of 1952–2010 and the same 10 ensemble members as the rainfall data was used from d4PDF-AGCM. 850 hPa daily mean temperature and specific humidity used to calculate the monsoon front location. Zonal wind, meridional wind and specific humidity at pressure levels 1000, 925, 850, 700, 600
155 and 500 hPa were used to calculate water vapour flux.

2.1.4 Processing tools

Coastlines and administrative boundaries were obtained from the Database of Global Administrative Areas version 4.1
160 (GADM; https://gadm.org). Principle Component Analysis and part of the data processing was carried out using Max-Planck Institute for Meteorology's Climate Data Operators software package (CDO; Schulzweida, 2022). Equivalent potential temperature was calculated using the NCAR Command Language (NCL, 2019). The rest of the data processing was carried out in Python 3, using python libraries NumPy (Harris et al., 2020), SciPy (Virtanen et al., 2020), pandas (McKinney, 2010) and xarray (Hoyer and Hamman, 2017). In particular, clustering of rainfall and curve fitting was carried out using Scipy.
165 Figures were prepared with the python libraries Matplotlib (Hunter, 2007) and Cartopy (Met Office, 2010–2015).

2.2 Method

2.2.1 Processing tools

170 The SST field from COBE-SST was cropped to the domain of 100°E–60°W, 20°S–60°N. SST anomalies were calculated by subtracting the long-term monthly mean of the analysis period from the monthly SST, at each grid-point. The anomalies were areal-weighted with the cosine of latitude. Principle Component Analysis (PCA) was performed on the concatenation of five seasonal mean anomalies, centered on the JJA season of the indexed year, i.e. the sample of 1952 would consist of dJF (December 1951, January 1952, February 1952), MAM (March 1952, April 1952, May 1952), JJA (March 1952, April
175 1952, May 1952), SON (September 1952, October 1952, November 1952), and Djf (December 1952, January 1953, February 1953) seasonal mean anomalies. The anomalies were not standardised before PCA. PCA with time concatenation has been used in past studies to obtain the time evolution patterns of Pacific SST anomaly modes (Weare and Nasstrom 1982, Guan and Nigam 2008). The PCA was performed for the 71-year period of 1952–2022 based on JJA, i.e. using data from December 1951 to February 2023.
180

After PCA, areal-weighting was removed. Standardised scores (scores) and loadings were calculated from the Principle Components (PC) and Empirical Orthogonal Functions (EOFs), i.e. each PC (EOF) was divided (multiplied) by the square root of its corresponding eigenvalue to give the score (loading), so that the strength of the loading indicates its contribution to the total variance of temperature anomalies. A varimax rotation was performed on the 29 top modes and the rotated modes
185 reordered by their explained variance. Twenty nine modes were used for rotation following Guan and Nigam (2008), who selected this number based on the number of modes being above "noise level".

2.2.2 Rainfall clustering

190 Upper percentile rainfall in June–July of every year was calculated for individual grid-points of the gridded datasets, and for each individual rain-gauge. For d4PDF, this was calculated for each individual ensemble member. The percentile calculation was inclusive of times with zero rainfall. For hourly rainfall, Ph_{99} was the 15th highest value. For daily rainfall, Pd_{90} was the sixth highest value. This produced time series of 71, 17, and 59 samples (years), for rain-gauges, radar-AMeDAS, and d4PDF. The exceptions were the rain-gauges at Fukuoka (68 years), Shionomisaki (67 years), and Nara (70 years). The
195 ensemble mean was taken for d4PDF.

The spatial points were clustered using the Hierarchical Density-Based Spatial Clustering of Applications with Noise (HDBSCAN) function, Scipy's implementation of the hierarchical density-based clustering algorithm developed by Campello et al. (2013). In this algorithm, a hierarchical tree of all the samples is first built by searching around the vicinity
200 of each point at increasing radius based on a distance metric, merging them into larger and larger clusters, until a single cluster that includes all points is formed. The most persistent clusters along the depth of the tree that fulfill the user-provided minimum cluster size (c_{min}) are finally selected. We defined the distance metric between two points as $D = 1 - R$ if the Spearman correlation R was statistically significant at $\alpha=0.05$ and the two points were neighboring points, $D=2.0$ otherwise. The tree-construction algorithm was set to brute-force ("brute"), i.e. the tree was explicitly constructed without
205 the use of approximations to speed up calculation. The minimum sample size (a different parameter from c_{min}) was set to c_{min} =1, i.e. clusters could keep expanding as long as one more sample could be added. The initial setting was c_{min}=3, i.e. only clusters of more than three points would be returned. This setting is explained below.

Since we were unable to cluster radar-AMeDAS at full resolution due to computation limitations, the sample size was
210 incrementally doubled, implemented through randomly selecting a point in each 16×16, 8×8, 4×4 set of grid-points. After a 16-fold sample reduction (4×4 set), radar-AMeDAS could be clustered. Neighboring points were determined through Delaunay triangulation, so the algorithm was set to return at least one triangle (three samples, or c_{min}=3). The reduced resolution radar-AMeDAS was clustered a few times, each time with new randomly selected points. Western Japan was divided into eight pieces of approximately the same size, roughly following the regional patterns from the reduced resolution
215 data. The individual pieces were clustered at full resolution. In the case of gridded-data at full resolution, neighboring points were the eight grid-points surrounding any grid-point. Clustering with different values of c_{min} was then tested.

Since d4PDF clustered at full resolution, western Japan was clustered as a single piece using different values of c_{min}.

220 For each cluster or unclassified point ("set"), a time series of rainfall extreme was calculated. At each timestep, the maximum rainfall at each set was selected. For example, in a cluster of three points, this would be the point with the highest rainfall and the other two points would be discarded. This was based on the concept that a set included locations which experienced rainfall from the same event, and the maximum rainfall of that event was sampled by a rain gauge that could "see" the entire location rather than only one specific point. The number of samples every year would also be only along the
225 time dimension and remain the same between different sets for the calculation of percentile rainfall. Ph_{99} and Pd_{90} were then calculated every year for each set. Spearman correlation was calculated between the time series of extreme rainfall of each set, and the score of each mode from the rotated PCA.

2.2.3 Selection of analysis regions

Radar-AMeDAS and d4PDF at both hourly and daily timescales produced four cluster patterns, but the identical spatial extents have to be used when comparing between datasets or timescales. Ten rectangular regions of approximately the same area were selected over western Japan, such that they approximately covered areas of similar correlation signs. Their longitudinal and latitudinal extents are listed in Table 1, and shown in Supp. Fig. S2-2. For each region, the percentile rainfall each year was calculated using two methods, which will be referred to as the "sets" and "box" methods. In the sets methods, both spatial and temporal samples were used in the percentile calculation. For example, a region containing 10 sets (either clusters or unclassified points) over 61 days in June–July would have a sample size of 610 daily samples per year. In the box method, the box was considered as a single set, i.e. the maximum rainfall in the box was selected at each hourly or daily timestep, and only temporal samples were used in the percentile calculation. For example, each of the regions would always have 61 daily samples per year. Spearman correlation was again calculated between the time series of extreme rainfall of each region, and the score of each mode from the rotated PCA. As a robustness check on the correlation, this was repeated using the 99.9th upper percentile for hourly rainfall ($Ph_{99.9}$) and 99th upper percentile for daily rainfall (Pd_{99}).

The study was focused on the "sets" method, but the results of the "box" method were also calculated for comparison. The "box" method had the advantage that the total number of samples was standard across the regions by timesteps, but it was less reasonable to combine grid-points of different correlation to the SST modes. In this study, this was less of a concern, because the rectangular regions were selected based on correlation patterns; however, note that the selection was based on a posteriori knowledge of the spatial patterns after clustering. A third method of calculation was possible, which was to treat all grid-points and timesteps as individual samples, i.e. similar to the "sets" method but with all sets the size of one grid-point. This method was not used since it would combine the disadvantages of both methods; the sample size would now vary by spatial extent, and also combine grid-points of similar and dissimilar correlation to SST modes.

Table 1. The ten regions in western Japan selected for analysis. Regions are shown in Supp. Fig. S2-2.

Region	Label	Longitudinal extent (°E)	Latitudinal extent (°N)
1	KYUS	130.0 – 131.5	31.0 – 31.8
2	KYUW	129.8 – 131.0	31.8 – 32.8
3	KYUN	129.5 – 131.0	32.8 – 33.6
4	KYUE	131.0 – 131.8	31.8 – 33.3
5	CHUW	130.7 – 132.7	33.8 – 34.4
6	CHUN	132.8 – 134.8	35.1 – 35.7
7	CHUS	132.8 – 134.8	34.3 – 34.9
8	SHIP	133.0 – 134.5	33.2 – 34.0
9	KANS	135.0 – 136.2	33.4 – 34.4
10	KANN	134.8 – 136.0	34.4 – 35.4

2.2.4 Evaluation of correlation coefficients (CCs)

A correlation coefficient (CC) can be evaluated based on its strength, statistical significance (significance), and robustness. The strength of the Spearman correlation coefficient R is defined as "perfect" if $|R| = 1.0$, "very strong" if $1.0 > |R| \geq 0.8$, "strong" if $0.8 > |R| \geq 0.6$, "moderate" if $0.6 > |R| \geq 0.4$, "weak" if $0.4 > |R| \geq 0.2$, and "no relation" otherwise. Statistical significance was tested at $\alpha=0.05$, such that the thresholds for statistical significance corresponded approximately to "weak" for rain-gauges, "moderate" for radar-AMeDAS, and "weak" for both d4PDF-RCM datasets. Robustness was tested between the CCs for radar-AMeDAS, and that for the rain-gauges over the same 17-year period as radar-AMeDAS. For the "sets" method, robustness was tested using CCs calculated with different upper percentile values from radar-AMeDAS:

S1. For the "sets" method, the direction of the relationship between CCs calculated using Ph_{99} and $Ph_{99.9}$ must be the same. Similarly for Pd_{90} and Pd_{99}.

S2. Multiple rain-gauges with relationships must be of the same direction.

S3. If both radar-AMeDAS and any rain-gauge showed relationship, they must be of the same direction.

S4. If only radar-AMeDAS showed relationship, no more than half of the rain-gauges can have CCs of the opposite sign. For example, if radar-AMeDAS showed weak positive CC, and there were three rain-gauges, only one CC can be negative in value.

S5. If any of the rain-gauges showed relationship but not radar-AMEDAS, the correlation coefficient from radar-AMeDAS must be of the same sign.

To draw conclusions based on both short-term (17-years) and long-term (71-years) observations, CCs from radar-AMeDAS were compared with CCs from 71-years of rain-gauge, according to the following criteria:

L1. If neither radar-AMeDAS nor any of the long-term rain-gauges showed any relationship, there was "no relation" for the region.

L2. Multiple long-term rain-gauges with relationships must be of the same direction. (Similar to S2.)

L3. If both radar-AMeDAS and any long-term rain-gauge showed relationship, they must be of the same direction. (Similar to S3.)

L4. If only radar-AMeDAS showed relationship, no more than half of the long-term rain-gauges can have CCs of the opposite sign. (Similar to S4.)

L5. If any of the long-term rain-gauges showed relationship but not radar-AMEDAS, the correlation coefficient from radar-AMeDAS must be of the same sign. (Similar to S5.)

2.2.5 Monsoon activity indices

The structure of the monsoon front during a heavy rainfall episode has been described by Matsumoto et al, (1971) as being characterised more so by a low-level jet than temperature gradient, with heavy rainfall brought about by with mesoscale
300 systems associated with 1000 km wavelength disturbances. Indices aimed at describing the location, strength and stability of the low-level jet and the monsoon front were defined for two zonal ranges of 125–130 °E and 130–135 °E, which cover the region west of and over the analysis region, respectively.

The meridional and zonal components of the lower tropospheric water vapour flux (henceforth, just "wv-flux") at each grid-
305 point were calculated for each day by vertically integrating the product of daily mean specific humidity q and vector wind (u,v) through six pressure levels, 1000 hPa, 925 hPa, 850 hPa, 700 hPa, 600 hPa, and 500 hPa. In a discrete form, the zonal wv-flux is $\sum_i (q_i u_i + q_{i+1} u_{i+1}) (p_{i-1} - p_i) / 2g$, for $i=1...5$ pressure levels. The magnitude of the wv-flux was calculated from its zonal and meridional components. At each discrete longitude value, the discrete latitude location of the maximum wv-flux was located, then the zonal and meridional components were extracted at that location. The mean of the wv-flux jet latitude
310 and wv-flux components were calculated over the western and eastern (analysis) zonal ranges to obtain the daily time series ^{W}JLat, (^{W}QU, ^{W}QV), ^{E}JLat and (^{E}QU, ^{E}QV), respectively.

The daily location of the monsoon front was determined based on the methodology of Li et al. (2018). The 850 hPa equivalent potential temperature θ_e was calculated from daily mean temperature and specific humidity based on equation 39
315 of Bolton (1981). At each discrete longitude value, the latitudinal rate of change of θ_e, $(\partial \theta_e/\partial \varphi)_\lambda$, was then calculated. The monsoon belt was defined as present in the latitudes where $(\partial \theta_e/\partial \varphi)_\lambda \leq$ -0.04 K km^{-1}, and the location of the front was defined as the mean latitude if more than one latitude point was found. If only one latitude point was found, then the front was defined as not present. After this, the presence of the front was checked at the two points directly west and east of each longitude point. If the front was absent at both sides, then the front was defined as not present at the central point. The mean
320 of the front latitude was calculated over the western and eastern (analysis) zonal ranges to obtain the daily time series ^{W}FLat and ^{E}FLat, respectively.

For each of the 61 days in June–July, the mean of each index was taken over all the years of data, to obtain a 61-day time series. For d4PDF, this was done individually for each of the 10 ensemble members, to obtain 10×61=610 days. Individually
325 for either western or eastern zonal ranges, the time series QU and QV were fitted to sine functions Asin[π(t-T)/L]+B, with A, B, L and T as fit parameters. The time series JLat and FLat were fitted to logistic functions A[1 + e$^{-k(t-T)}$]$^{-1}$+B, with A, B, k and T as fit parameters. The fits were defined to be the climatological seasonal cycles (QU)$_0$, (QV)$_0$, (JLat)$_0$, and (FLat)$_0$. For any day of any year, the deviation from the climatological seasonal cycle was calculated to obtain anomalies (QU)$_a$, (QV)$_a$, (JLat)$_a$, and (FLat)$_a$. For example, (QU)$_a$ = QU - (QU)$_0$. For each year, the seasonal means μ_{QU}, μ_{QV}, μ_{JLat}, μ_{FLat}, and seasonal
330 variances $\sigma^2_{Q(U,V)}$, σ^2_{JLat}, σ^2_{FLat} were calculated from the anomalies to obtain seven annual time indices. For d4PDF, the indices were calculated individually for each member of the ensemble, then the ensemble mean was taken. For example, $\sigma^2_{Q(U,V)} = [\ \sum_i (\sigma^2_{QU} + \sigma^2_{QV})_i\ ]/N$ for $i=1...N$ ensemble members (N=10).

3 Results

335 ## 3.1 Principal Component Analysis (PCA) of Pacific SST anomalies

The top five modes appeared distinct from the remaining modes in terms of explained variance. These modes explained 26%, 16%, 9%, 7%, and 5% of total variance, while the remaining modes each explained 3% or less of the total variance (Supp. Fig. S1-0). The modes were similar to those from Guan and Nigam (2008), which had identified the first four modes of their rotated eigenvectors as ENSO+ (growth), ENSO- (decay), Trend, and Pan-Pacific Decadal Variability. In this study, the
340 relationships between rainfall extremes and the first fours modes were evaluated. These modes will be termed canonical ENSO growth (ENSO+), canonical ENSO decay (ENSO-), Trend-containing (Trend+), and Pacific Decadal Variability (PDV). Figures 1 and 2 show the loadings and scores, respectively.

The spatial loading Trend+ was not homogenous but showed seasonal and spatial variability, with cool anomalies over the
345 tropical Pacific resembling the La Niña and warm anomalies over the northwest Pacific (Fig. 1k-o). Although the Niña-like pattern was consistent with some past studies, other studies have also reported a Niño-like pattern, with the direction of the pattern depending on the choice of data used (e.g. Vecchi et al. 2008, Lee et al. 2022). The authors found the score and loading of the Trend+ mode to be sensitive to the analysis period, as well as whether COBE-SST or COBE-SST2 was used (Supp. Sect. 1). Comparing between the scores of Trend+ from COBE-SST and COBE-SST2, the overall warming trends
350 between 1960 and 2020 were similar, but the variability was quite different with a Spearman CC of only 0.65 (Supp. Fig. S3-3a). In contrast, the scores of other three modes were almost identical with CCs of greater than 0.96 (Supp. Figs S3-1a, S3-2a, S3-4a). From Fig. 2c, although the score of Trend+ overall increased in the analysis period, different interannual and decadal variability could be seen, which may contribute to the lower CC. Hence, mode 3 was termed "Trend-containing" rather than "Trend". Comparing between the loadings of Trend+ from COBE-SST and COBE-SST2, the spatial inhomogeneity from
355 COBE-SST appeared weaker, specifically in terms of warming of the northwest Pacific (Supp. Fig. S3-3b). Considering that the score from COBE-SST also appeared smoother, with less interannual and decadal variability, much of the patterns in Fig. 1k-o may be residue from interannual and decadal variability. The actual global warming pattern associated with only the warming trend may be much more homogenous.
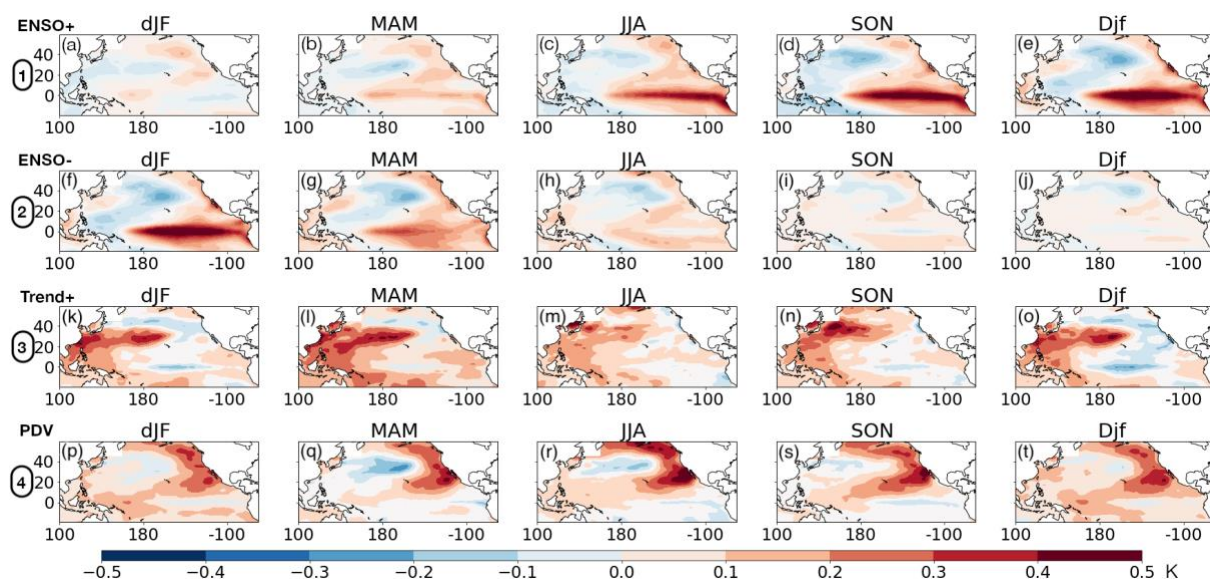
360
Figure 1. Loadings of the first four modes from the rotated Principal Component Analysis of Pacific sea surface temperature anomalies during years 1952–2022. Rows show the modes. Row 1 (a-e): ENSO-growth mode (ENSO+); row 2 (f-j): ENSO-decay mode (ENSO-); row 3 (k-o): Trend-containing mode (Trend+); row 4 (p-t): Pacific Decadal Variability mode (PDV). Columns show anomalies of five seasons centered on June-July-August (JJA).
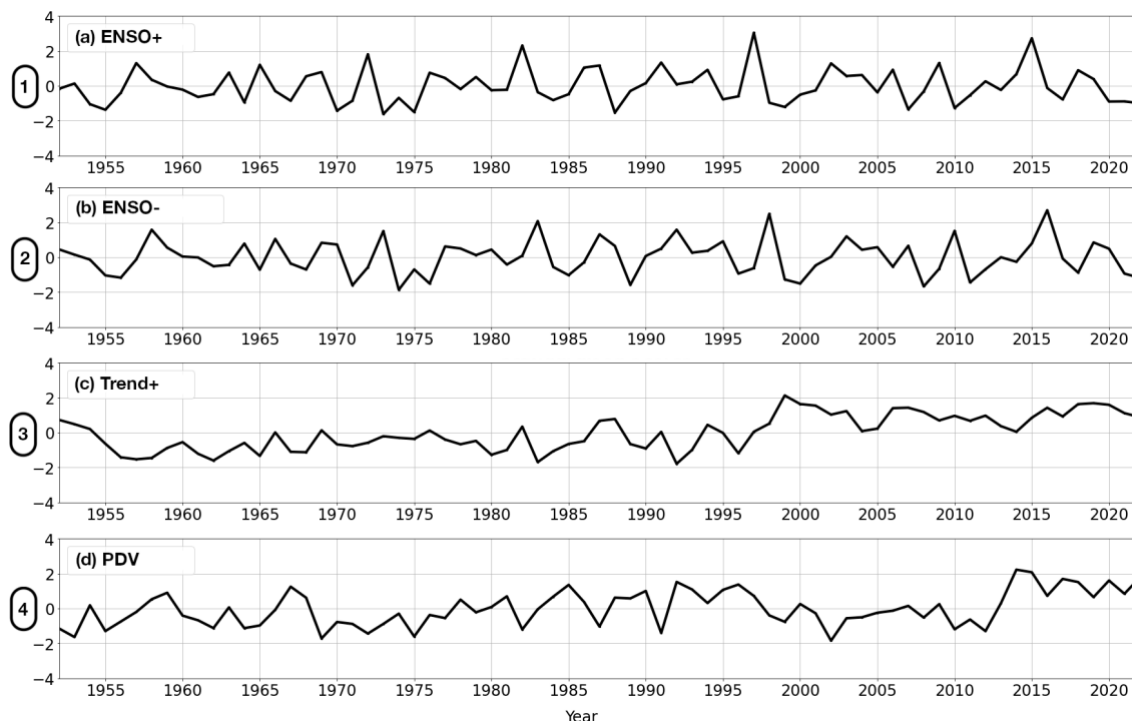
Figure 2. Scores of the first four modes from the rotated Principal Component Analysis of Pacific sea surface temperature anomalies during years 1952–2022: (a) ENSO-growth mode (ENSO+); (b) ENSO-decay mode (ENSO-); (c) Trend-containing mode (Trend+); (d): Pacific Decadal Variability mode (PDV).

3.2 Rainfall clustering

In the iterative clustering tests, the number of clusters decreased as c_{min} was increased, until all points merged into one cluster. This typically happened suddenly when a c_{min} threshold was crossed, because the number of neighboring points with significant CCs became less than c_{min}. At this point, the points would be clustered at D=2.0, returning one large cluster which contained all the points. For example, for Ph$_{99}$ over the north Kyushu piece of radar-AMeDAS, 216 clusters were returned at c_{min}=20, but only one cluster was returned at c_{min}=21 which contained almost all the points, and the remaining points were returned as unclassified. Over the south Kyushu piece of radar-AMeDAS, 148 clusters were returned at c_{min}=23, which suddenly dropped to six clusters at c_{min}=24, with one cluster containing almost all the points over land, the other five over the ocean, and remaining points unclassified.

The patterns obtained were similar (Supp. Figs S4-1 to S4-4), with higher c_{min} having the advantage of fewer and larger clusters for analysis, but having the disadvantage of more points being returned unclassified since they could not form sufficiently large clusters. We decided to select larger clusters and chose the values of c_{min} before the threshold was reached (Supp. Table S4-1). The results are shown in Fig. 3. In these figures, the numerical values and colors are only labels for the clusters from 1 up to the total number of clusters produced, so the spatial patterns of how similar clusters are arranged are more important than the specific colour of the cluster. Instead of the threshold value, c_{min} for d4PDF Pd$_{90}$ was set to the approximate value for Ph$_{99}$ (Figs 3b and 3d). This was because it was difficult to find the exact threshold for both Ph$_{99}$ and Pd$_{90}$. Kyushu and the western side of Chugoku would merge first while other regions remained distinct. Extremely large clusters would form over this whole western region and along the Pacific side of western Japan, while large regions also became unclassified. We decided on c_{min}=18, the value before the clusters over Kyushu island merged.

390

From Fig. 3, similar clusters were generally aligned with the long axis and coasts of western Japan. Such patterns were seen in d4PDF, except that the clusters were larger and smoother spatially. This was not surprising because each d4PDF grid was 25 times a radar-AMeDAS grid, so the higher resolution topographic impact of rainfall would not be explicitly simulated. The 5 km resolution produced more realistic patterns compared to the 20 km version of d4PDF, where each grid was 400

395   times a radar-AMeDAS grid (Supp. Fig. S4-5).
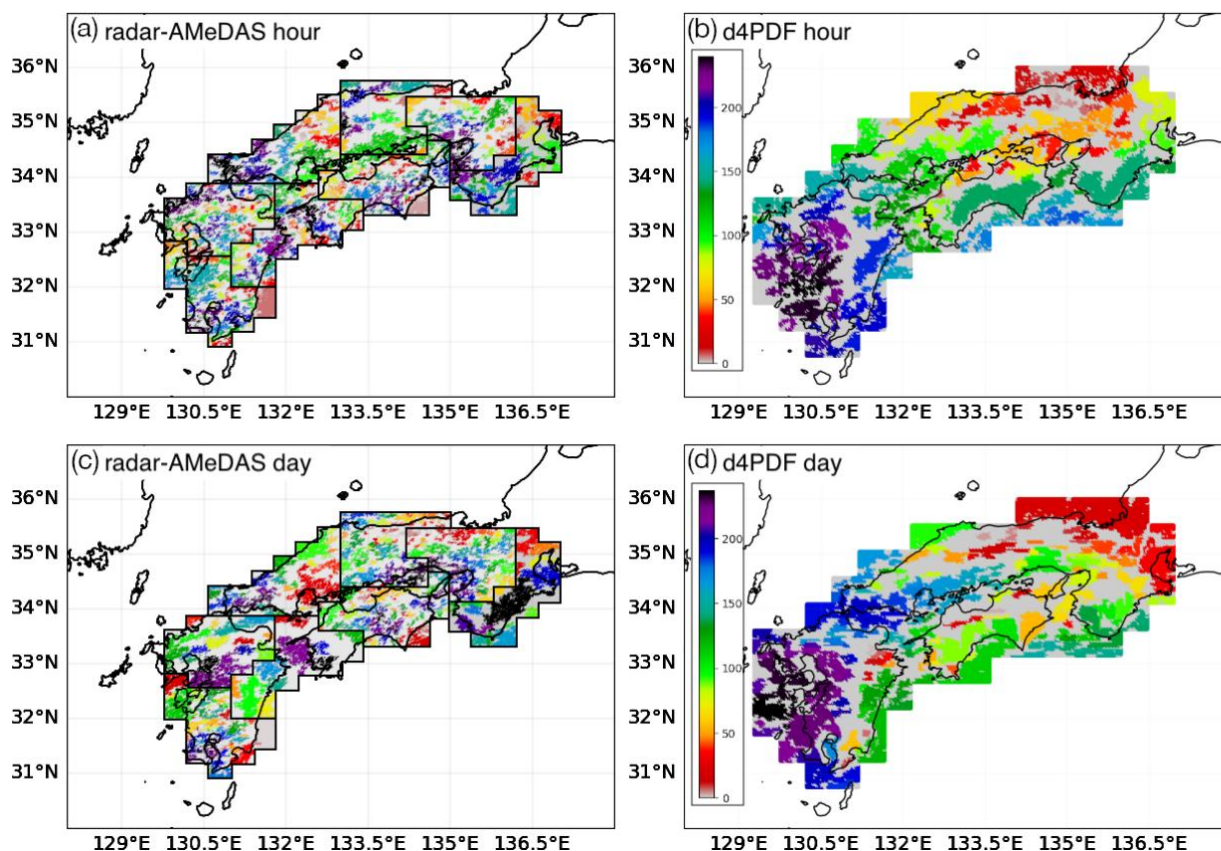
Figure 3. Labels of clusters based on (left column) the time series of seasonal 99th percentile hourly rainfall, (right column) seasonal 90th percentile daily rainfall. Colours only reflect the cluster numbering and do not reflect any units or magnitudes. Top
400   **row (a-b): 1 grid-point randomly selected every 4×4 grid from radar-AMeDAS; (c-d): d4PDF 5 km RCM; (e-f) d4PDF 20 km RCM. Radar-AMeDAS and d4PDF-RCM time periods are 2006–2022 and 1952–2010, respectively.**

3.3 Correlation values

Figs 4 and 5 show the Spearman CCs between the rainfall extremes of the sets (clusters or points) and the scores of the four
405   Pacific SST modes, for hourly and daily extremes, respectively. Since there was a possibility that the strong correlation could be due to tropical cyclones (TCs), the CCs were recalculated after setting rainfall to zero during days with possible be TC influence (Supp. Sect. 5). The spatial patterns remained similar, though CCs sometimes weakened or strengthened. The only notable land region that showed strong CCs both with and without TCs was at the southern tip of Kyushu, for correlation of ENSO- with Ph_{99} (box 1 in Fig. 4c) and Pd_{90} (box 1 in Fig. 5c).

410

The relationships were summarised for the 10 regions defined in Sect. 2.2.3, using the evaluation criteria listed in Sect. 2.2.4 (Table 2). The correlation values are shown in Supp. Sect. 6. The direction of relationships was generally consistent between the "sets" and "box" methods; 66 of 80 pairs matched for observations (circles in Table 2), while 60 of 80 pairs matched for d4PDF (background in Table 2). For observations, the two methods matched completely in KYUN and KYUE. This was

415 followed by KYUS, KYUW, CHUW and KANN with one mismatch (of eight pairs). The other regions had two mismatches except for KANS with four mismatches. For d4PDF, the methods matched completely in CHUW, had one mismatch in KYUN and CHUN, and two mismatches in KYUS, KYUW, KYUE and SHIP. They were most discrepant in KANN with four mismatches. Overall, most consistent areas were the CHUN, CHUW, and the Kyushu regions (1–3 mismatches), while the least consistent were CHUS and the Kansai areas (5–7 mismatches).

420

Radar-AMeDAS and rain-gauges for the same 17-year period were almost always consistent, i.e. did not violate criteria S3–S5 of Sect. 2.2.4. Hence, each SST mode were compared in two ways: firstly, observation-based correlation patterns were compared for the 17-year and 59-year periods; and secondly, correlation patterns were compared between d4PDF and observations. For the 59-year period of d4PDF, weak CCs were still significant, so the performance of model was evaluated

425 based how consistent its correlation patterns were with rain-gauges, even for weak CCs. Correlation patterns in d4PDF were generally similar between Ph_{99} and Pd_{90}, so the descriptions of d4PDF apply to both timescales.

ENSO growth mode (ENSO+): Observed relationships with rainfall extremes were consistent between time periods (Figs 4a vs 4b; 5a vs 5b), with correlation over the northwestern Kyushu and western Chugoku regions, but weak anti-correlation

430 over the Pacific coast. d4PDF was consistent with observations, but was spatially biased. The regions of weak correlation were shifted northeast in the model to Chugoku and Kansai (boxes 4–10 in Fig. 4b; boxes 6–10 in Fig. 5b). There may also be regions of weak anti-correlation over southern Kyushu to western Shikoku.

ENSO decay mode (ENSO-): Observed relationships with rainfall extremes were partially consistent between time periods

435 (Figs 4c vs 4d; 5c vs 5d), with weak correlation over southern Kyushu, but weak anti-correlation over eastern Kyushu and some coastal regions. The weak-to-strong correlation observed over many regions for the 17-year period was not observed for the 59-year period (different rain-gauges near box 1, 2, 3, 5 in Figs 4c and 5b). On the other hand, weak anti-correlation was observed for both periods in the central and east regions of Kyushu (boxes 2 and 4 in Figs 4c, 4d and 5c; box 3 in Fig. 5d), the eastern regions Chugoku (box 7 in Figs 4c and 4d, but not in Figs 5c and 5d) and the region east of Kansai

440 (inside/east of box 10 in Figs 4c, 5c and 5d, but not Fig. 4d). d4PDF was consistent with observations, but biased towards positive correlation. d4PDF showed weak-to-moderate correlation in most of the study domain, similar to but also more positive than the 17-year observations. Close to the observed anti-correlated regions, d4PDF also showed weak anti-correlation or no-relation, i.e. in eastern Kyushu (box 4), Shikoku (box 8), and the east of southern Kansai (east of box 9).

445 **Trend-containing mode (Trend+):** Observed relationships with rainfall extremes were consistent between time periods, with up to strong correlation for the 17-year period and weak correlation for the 59-year period, along the Pacific side of the islands (inside/near boxes 1, 4, 8, 9 in Figs 4e, 4f, 5e and 5f). d4PDF was consistent with observations. Weak correlation was also seen in d4PDF at the Pacific side (boxes 1–3, 8, 9 in Fig. 4f; boxes 1, 2, 8 in Fig. 5f), but the spatial extent of these regions were smaller than observed.

450

Pacific Decadal Variability mode (PDV): Observed relationships with rainfall extremes were consistent between time periods, but with a spatial shift. For the 17-year period, weak-to-moderate anti-correlation was observed more along the Sea of Japan side, while weak correlation was observed along the Pacific coast in southern Kyushu (box 1 in Figs 4g and 5g) and Shikoku (box 8 in Fig. 5g, but not Fig. 4g). For the 59-year period, weak anti-correlation was observed along the Pacific

455 coast instead (two gauges near box 8 in Fig. 4h; 10 gauges near boxes 1, 4, 8 and 10 in Fig. 5h). d4PDF was inconsistent with observations, showing no anti-correlated region. However, d4PDF showed weak correlation along the Pacific coast in southern and eastern Kyushu, Shikoku (Pd_{90} only), and southern Kansai (boxes 1, 2, 4, 8–10 in Fig. 4h; boxes 1, 4, 8–10 in Fig. 5h).
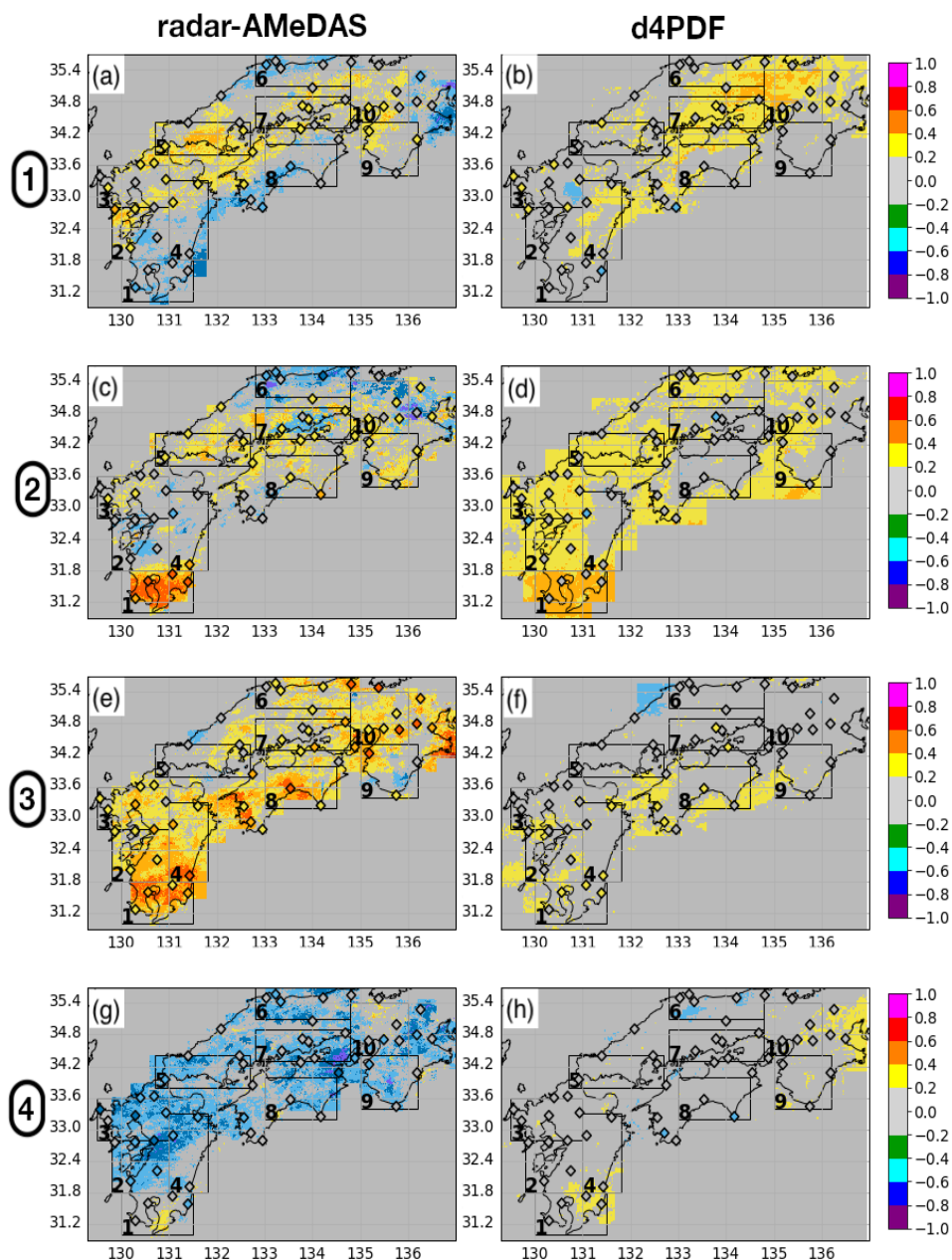
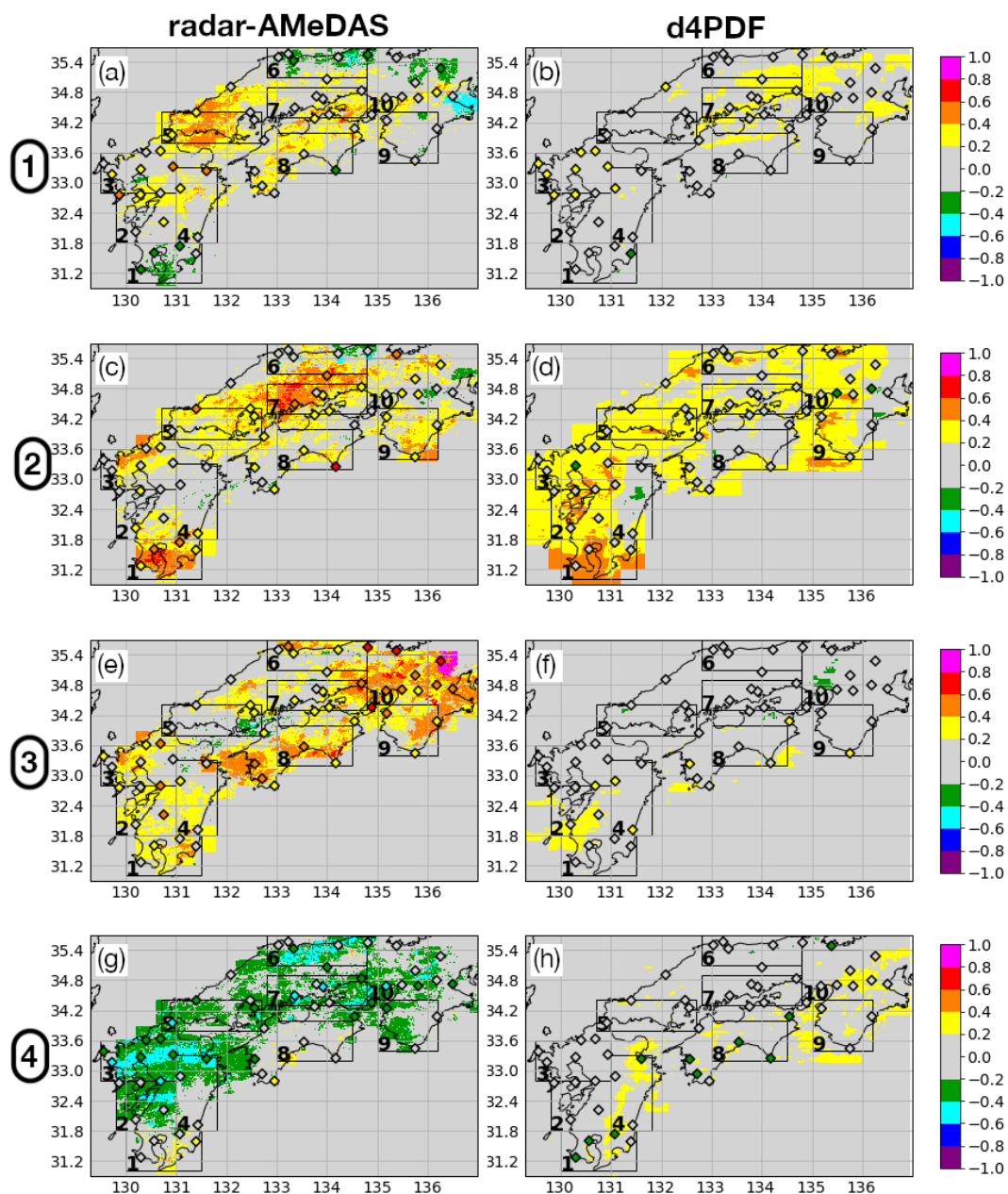**Figure 4. Shading shows Spearman CCs between the scores of four Pacific SST modes (numbered rows) and seasonal 99th percentile hourly cluster rainfall from (left column) radar-AMeDAS and (right column) d4PDF. (a) ENSO+ with radar-AMEDAS; (b) ENSO+ with d4PDF; (c) ENSO- with radar-AMEDAS; (d) ENSO- with d4PDF; (e) Trend+ with radar-AMEDAS; (f) Trend+ with d4PDF; (g) PDV with radar-AMEDAS; (h) PDV with d4PDF;. CCs were calculated for each cluster, each of which contains multiple grid-points, and the grid-points belonging to the same cluster were colored identically. Radar-AMeDAS and d4PDF time periods are 2006–2022 and 1952–2010, respectively. Coloured diamonds show CCs calculated from rain-gauges for the same period as the panel they appear in, either 2006–2022 for radar-AMeDAS panels, or 1952–2010 for d4PDF panels. Numbered boxes show the 10 analysis regions defined in Table 1.**

460

465

Figure 5. The same as Fig. 4, except for the seasonal 90th percentile daily cluster rainfall from (left column) radar-AMeDAS and (right column) d4PDF.

Table 2. Strength of Spearman CC between rainfall extremes in the 10 analysis regions (rows) and the scores of four Pacific SST modes (columns). For each region, CC strengths for seasonal 99th percentile hourly rainfall and 90th percentile daily rainfall are shown using the same colors as Figs 4 and 5. Square backgrounds show results from d4PDF, while circles show results from observations. Double square frames and double circles indicate statistical significance at α=0.05. When the circle is the same color as the background, the double circle for statistical significance is drawn as a black circle. The only strong positive CCs (red circles) are observed in ENSO- with KYUS (hourly sets), and Trend+ with SHIP (hourly sets, daily sets), while the all other instances of the same red-green tone are green.

4 Discussion

The lack of strong CCs between rainfall extremes and Pacific climate variability suggests that the latter is not necessarily a controlling factor for the former. Extreme rainfall typically occurs in mesoscale systems which may be associated with
485 certain synoptic scale conditions, but are much less likely to be directly influenced by hemispheric or planetary scale climate variability. If the relationship is not direct, the correlation strength would not be strong. Possible indirect relationships are discussed below, using indices that describe the seasonal condition of the monsoon front (c.f. Sect. 2.2.5). Results using JRA55 will be considered to be "observation" here.

4.1 Relationships between monsoon activity and rainfall extremes

490 The CCs between rainfall extremes and monsoon jet strength were stronger over the 125–130 °E western range than over the 130–135 °E eastern range. The results for the western range are presented below and the notation simplified to mean zonal anomaly μ_{QU}, mean meridional anomaly μ_{QV}, and variance of the anomaly $\sigma^2_{Q(U,V)}$. The CCs calculated using monsoon jet and front latitudes were similar over both ranges. The results for the eastern range are presented below and the notation simplified to mean jet latitude μ_{JLat}, variance of the jet latitude σ^2_{JLat}, mean front latitude μ_{JLat}, and variance of the front
495 latitude variance σ^2_{JLat}. Table 3 shows the strength of the CCs between rainfall extremes and the indices, which summarises the results both with radar-AMeDAS for the 17-year short-term period of 2006–2022 and with rain-gauges for the 53-year long-term period of 1958–2010 (Supp. Tables S7.1a, S7.1b, and S7.2).

Three hypotheses regarding the occurrence of extreme rainfall are evaluated. We here discuss these three hypotheses in
500 detail.

Hypothesis 1: The first possibility is that the convective systems were more intense and produced stronger extreme rainfall. Higher μ_{QU} (μ_{QV}) represents stronger eastwards (northwards) water vapour entering Japan. Both observation and simulation indicate that this was associated with stronger rainfall extremes.

505
With μ_{QU} (column 1 in Table 3), weak-to-strong correlation was observed in all regions except CHUN. This was particularly notable in KYUS, KYUW and KYUE, where 22 of 24 rain-gauge hourly and daily CCs showed weak-to-moderate correlation. In comparison, d4PDF showed weak-to-moderate correlation in Kyushu and Chugoku, except KYUE. With μ_{QV} (column 2 in Table 3), weak-to-strong correlation was observed in Kyushu and Chugoku. This was particularly notable in
510 KYUN, CHUW, and CHUN. In CHUW, weak-to-moderate correlation was observed at all rain-gauges. In KYUN and CHUN, weak correlation for Pd_{90} was observed at all but one rain-gauge in each region. In comparison, d4PDF showed weak-to-strong correlation in all 10 regions.

Hypothesis 2: The second possibility is that a region experienced stronger extreme rainfall because of the monsoon front
515 was in a position such that more convective systems moved over the region. The indices representing the position of the monsoon jet (μ_{JLat}) and front (μ_{FLat}) are indicators of this. Neither was observed to be associated with rainfall extremes except in KYUW for μ_{JLat} and KYUS for μ_{FLat}. In d4PDF, a more southern monsoon jet was associated with stronger rainfall extremes over the Pacific coast.

520 With μ_{JLat} (column 4 in Table 3), only three of 38 rain-gauges showed any relationship for the 53-year period, and all three of these rain-gauges were in KYUW showing weak anti-correlation. In contrast, d4PDF showed weak-to-moderate anti-correlation in eight regions, except for KYUN and CHUW. With μ_{FLat} (column 6 in Table 3), only eight of 38 rain-gauges showed any relationships for the 53-year period. Three of these eight rain-gauges were weakly anti-correlated in KYUS. d4PDF also showed weak anti-correlation in KYUS, CHUS, CHUN, and KANN. In CHUS and KANN, the direction of the
525 relation was reversed compared to observation.

17

Table 3. Strength of Spearman CCs between rainfall extremes in the 10 analysis regions (rows) and indices describing the monsoon front (columns). The CCs are shown using the same colors as Figs 4 and 5. The columns are for the mean zonal component of the monsoon jet water vapour flux anomaly μ_{JQU}, mean meridional component of the monsoon jet water vapour flux anomaly μ_{JQV}, variance of the monsoon jet water vapour flux $\sigma_{JQ(U,V)}$, mean monsoon jet latitude μ_{JLat}, variance of the monsoon jet latitude σ_{JLat}, mean monsoon front latitude μ_{FLat}, and variance of the monsoon front latitude σ_{FLat}. For each region, sub-rows are for seasonal 99th percentile hourly rainfall and 90th percentile daily rainfall. Square backgrounds show results from d4PDF, while circles show results from observations. Double square frames and double circles indicate statistical significance at α=0.05. When the circle is the same color as the background, a black circle is used for statistical significance.

Hypothesis 3: The third possibility is that disturbances occurred more frequently in a season, increasing the possibility of stronger extreme rainfall. The variance indices ($\sigma^2_{Q(U,V)}$, σ^2_{JLat}, σ^2_{FLat}) are indicators of this. Higher $\sigma^2_{Q(U,V)}$ represents the

540 more disturbances in the water vapour flux of the monsoon jet west of the study region, while higher σ^2_{JLat} and σ^2_{FLat} represent more disturbances over Japan. However, both observation and simulation indicate the reverse was true, that stable monsoon jet strength $\sigma^2_{Q(U,V)}$ and latitude σ^2_{JLat} was associated with higher rainfall extremes. The association was much stronger in d4PDF.

545 With $\sigma_{Q(U,V)}$ (column 3 in Table 3), weak-to-moderate anti-correlation was observed in KANS and Kyushu except KYUN, while weak correlation was observed in CHUN and CHUS. The relationship was particularly notable in KYUS, where weak-to-moderate anti-correlation was observed at all rain-gauges. In the four observed anti-correlated regions, d4PDF showed weak-to-moderate correlation in KYUE and no-relation in the rest. It showed weak correlation in the observed correlated regions of CHUN and CHUS, as well as SHIP and KANN. This suggested that stable water vapour flux in the monsoon jet

550 was associated with stronger rainfall extremes over KYUS and KYUW, but with weaker rainfall extremes in the other regions. d4PDF was biased towards correlation or the latter effect.

With σ_{JLat} (column 5 in Table 3), weak-to-moderate anti-correlation was observed in all 10 regions. In d4PDF the relationship was much stronger, with moderate-to-strong anti-correlation in all 10 regions, except for Ph_{99} in SHIP where the

555 relationship was weak. With σ_{FLat} (column 7 in Table 3), only two rain-gauges showed weak anti-correlation for the 53-year period. d4PDF showed weak anti-correlation in Kyushu, CHUW, SHIP, and KANS (Ph_{99} only).

4.2 Relationships between Pacific SST modes and monsoon activity

Table 4 shows the strength of the CCs between the indices and the scores of the Pacific SST modes. JRA55 and d4PDF were

560 compared for the period of 1958–2010, JRA55 CCs were similar between the periods of 1958–2010 and 1958–2022 (Supp. Table S7.3a), and d4PDF CCs were similar between the periods of 1958–2010 and 1952–2010 (Supp. Table S7.3b). The explanations below summarize Supp. Tables 7.4a-d. Although two variables individually correlated with a third variable need not be themselves correlated, the relationship between the SST modes and regional rainfall could be partially explained using monsoon activity as the intermediary. Below, the focus will be on situations where both SST-monsoon and monsoon-

565 rainfall CCs were statistically significant.

ENSO+: For the 17-year (53-year) period, significantly strong (weak) correlation was observed with $\sigma_{Q(U,V)}$, resulting in an anti-correlated effect with rainfall extremes in KYUS and KYUW. Like observation, d4PDF showed significant weak correlation $\sigma_{Q(U,V)}$, but this would result in a correlated effect over KYUE. d4PDF also showed significant weak anti-

570 correlation with μ_{QV}, resulting in an anti-correlated effect over western Japan. This was opposite to observation, with non-significant moderate correlation with μ_{QV} for the short-term period only, resulting in a correlated effect over most of Kyushu and Chugoku. This explained why for the 17-year period correlation was observed over western Japan, except for southern Kyushu where there was anti-correlation. However, this did not explain the observed correlation for the 53-year period. Finally, d4PDF showed significant moderate (strong) anti-correlation with μ_{JLat} (μ_{FLat}), resulting in a correlated effect over

575 western Japan, particularly the eastern side of the study domain. These stacking effects explained why d4PDF showed no-relation or anti-correlation in the southwest, to correlation in the northeast.

ENSO-: For the 17-year (53-year) period, significant strong (weak) correlation was observed with μ_{QU}, resulting in a correlated effect with extreme rainfall over western Japan. For the 53-year (17-year) period, significant (non-significant)

580 weak correlation was observed with $\sigma_{Q(U,V)}$, resulting in a correlated effect in KYUS and KYUW. Like observation, d4PDF showed significant moderate correlation with μ_{QU}. d4PDF also showed significant moderate anti-correlation with σ_{JLat}, and both resulted in correlated effects. Non-significant moderate anti-correlation was observed with σ_{JLat} for the short-term period only, resulting in a correlated effect. The positive bias between ENSO- and rainfall extremes in d4PDF reflected the

much stronger relationships of rainfall extremes with both μ_{QU} and σ_{JLat}. This explained why the correlation patterns were more similar between d4PDF and 17-year observations, than either with 53-year observations.

Trend+: No pairs of statistically significant CCs were found. For the 17-year period only, weak correlation with μ_{QU} could explain the correlated effect with extreme rainfall over western Japan, but alternative mechanisms than the three hypotheses could also be responsible.

PDV: For the 53-year (17-year) period, significant (non-significant) weak anti-correlation was observed with μ_{QV}, resulting in an anti-correlated effect with extreme rainfall over western Japan. d4PDF did not show this relationship, which explained why anti-correlation with extreme rainfall was seen in observations but not in d4PDF.

From the above analysis, the relationships between the two ENSO modes and rainfall extremes could be explained by stronger water vapour flux along the jet (hypothesis 1) and more stable monsoon jet (refutation of hypothesis 3). The important monsoon indices differed with ENSO growth and decay, and by region. In contrast, the relationships with the Trend+ mode were poorly explained through the monsoon indices, since no pairs of statistically significant CCs were found. While a pair of significant CCs were found for PDV, the magnitudes were weak, comparable to those of Trend+.

Table 4. Strength of Spearman CCs between indices describing the monsoon front (rows) and the scores of four Pacific SST modes (columns), using different datasets and time periods. The CCs are shown using the same colors as Figs 4 and 5. The rows are for the mean zonal component of monsoon jet water vapour flux anomaly μ_{JQU}, mean meridional component of monsoon jet water vapour flux anomaly μ_{JQV}, variance of the monsoon jet water vapour flux anomaly $\sigma_{JQ(U,V)}$, mean monsoon jet latitude μ_{JLat}, variance of the monsoon jet latitude σ_{JLat}, mean monsoon front latitude μ_{FLat}, and variance of the monsoon front latitude σ_{FLat}. Bold font indicates statistical significance at $\alpha=0.05$.

			ENSO+			ENSO-			Trend+			PDV		
			2006-2022	1958-2010		2006-2022	1958-2010		2006-2022	1958-2010		2006-2022	1958-2010	
			JRA55	JRA55	d4PDF	JRA55	JRA55	d4PDF	JRA55	JRA55	d4PDF	JRA55	JRA55	d4PDF
West (125–130 °E)	wvjet Qflux	QU anomaly	-0.35	-0.20	-0.08	**0.72**	**0.31**	**0.47**	0.24	0.12	0.05	0.13	-0.13	-0.18
		QV anomaly	0.44	0.05	**-0.28**	0.25	0.03	**0.30**	0.11	0.17	0.13	-0.35	**-0.27**	0.07
		variance	**0.67**	**0.30**	**0.29**	-0.37	**-0.32**	-0.12	-0.17	-0.07	0.10	0.08	-0.02	0.10
East (130–135 °E)	wvjet latitude	anomaly	-0.35	-0.15	**-0.31**	0.30	0.17	-0.22	-0.26	-0.12	-0.06	-0.25	0.01	-0.10
		variance	-0.15	0.13	0.08	-0.41	-0.10	**-0.57**	-0.06	-0.03	-0.06	-0.06	0.05	-0.02
	front latitude	anomaly	0.06	-0.15	**-0.42**	-0.10	-0.24	**-0.28**	-0.04	-0.08	-0.13	-0.15	-0.17	0.03
		variance	-0.14	0.14	0.23	-0.28	0.06	-0.11	-0.22	0.21	-0.05	0.10	0.04	-0.14

5 Conclusion

610

This study investigated the relationships between the extreme rainfall over western Japan and the hemispheric-scale climate variability of Pacific basin SST. The representation of those relationships in the d4PDF climate ensemble was evaluated and compared to observed relationships, using the same methodology summarised below.

615 The annual 99th upper percentile hourly rainfall and the annual 90th upper percentile daily rainfall in 17 years (2006–2022) of radar-AMeDAS and 59 years (10-member ensemble mean of 1952–2010) d4PDF were clustered using the HDBSCAN algorithm, for western Japan. Rainfall clusters aligned along coasts and long axis of the islands were found in both observation (radar-AMeDAS) and model (d4PDF). Using each cluster as a spatial sample, Spearman correlation was calculated between the rainfall extremes and the scores of four modes of Pacific SST variability. The four modes were
620 obtained by the varimax rotation of extended PCA on Pacific SST anomalies from COBE-SST2, and reflected canonical ENSO growth, canonical ENSO decay, warming trend, and PDV. Correlation was also calculated using rainfall extremes from rain-gauges for the two time periods. Observed correlation strength was at most moderate ($|R| < 0.6$) over most of western Japan. The observed relationships were: both directions for ENSO growth, correlation with ENSO decay, correlation with warming trend, and anti-correlation with PDV. d4PDF reflected similar relationships for the first three modes, although
625 it showed both spatial and strength biases. The model was particularly biased towards positive correlation between ENSO decay and rainfall extremes. For the PDV mode, the model could not reproduce the observed relationship of spatially widespread anti-correlation with rainfall extremes. With respect to the inter-annual climate variability of rainfall extremes, the model has performed surprisingly well, but appears as yet only suitable for study domain-wide climate projections.

630 The authors next tried to explain the relationships through monsoon activity as an intermediary between the hemispheric-scale variability and the regional-scale rainfall. 14 monsoon activity indices were calculated from 64 years of (1958–2022) JRA55 and 59 years (10-member ensemble mean of 1952–2010) of d4PDF. For both of the regions west of Japan (125–130 °E) and over the study domain (130–135 °E), seven indices were calculated which reflected the seasonal mean and variability of the monsoon front latitude, the seasonal mean and variability of the monsoon jet latitude, the seasonal mean of
635 the zonal and meridional water vapour flux at the monsoon jet (jet strength), and the seasonal variability of the jet strength. The monsoon indices were correlated with rainfall extremes and the scores of the Pacific SST modes, with JRA55 considered to be observation. Weak or moderate correlation with monsoon jet indices was observed over many rain-gauges for the 53-year period (1958–2010). Strong correlation strength was observed only for the 17-year period. The relationship between the ENSO modes and rainfall extremes could be partially explained using indices related to the monsoon jet. In
640 particular, d4PDF's positive bias between rainfall extremes and ENSO decay could be explained by excessively strong anti-correlations of rainfall extremes with jet latitude variance, and of jet latitude variance with ENSO decay.

Three questions were posed in the Introduction, which are answered as follows:

645 Firstly, increasing the number of spatial rainfall samples through the use of radar probably would not result in much stronger correlations than found in rain-gauges. The moderate-strong correlations from radar-AMeDAS were due to the short analysis period of 2006–2022, since moderate-strong correlations were also seen from rain-gauges using the same time period. Nevertheless, the authors found that additional value was provided by radar-AMeDAS, because it confirmed that the weak-to-moderate CCs at individual rain-gauges were not by chance, but part of regional spatial patterns.
650

Secondly, the relationships between rainfall extremes and ENSO development stage indeed differed. Rainfall extremes were correlated with ENSO growth in northern Kyushu and Chugoku, but possibly anti-correlated along the Pacific coast. In contrast, rainfall extremes were correlated with ENSO decay in southern Kyushu, but possibly anti-correlated over east Kyushu and a few other coastal regions. Since the ENSO often oscillates between the El Niño and La Niña phases, an El
655 Niño transitioning into a La Niña may be interpreted as combining the effects of the ENSO- mode and the reversed effects of the ENSO+ mode, i.e. stronger rainfall extremes over southern Kyushu but weaker rainfall extremes over northern Kyushu. The relationships could be partially explained through the water vapour flux of the monsoon jet, such as due to stronger zonal water vapour flux and smaller flux variance in the above example jet. The stronger zonal water vapour flux is

660 consistent with Naoi et al. (2020) who found atmospheric rivers to be more frequent in years when El Niño transited into La Niña.

Thirdly, rainfall extremes were found to be weakly anti-correlated with Pacific Decadal Variability over many regions of western Japan, particularly Kyushu and Shikoku. While the effect of individual modes was weak, they may stack since the SST anomalies of the PDV were quite ENSO-like. A La Niña transitioning into an El Niño may be interpreted as combining 665 the effects of the ENSO+ mode and the reversed effects of the ENSO- mode, i.e. stronger rainfall extremes over northern Kyushu. Should this event also occur during the negative (Niña-like) phase of the PDV, the three modes would stack in their strengthening influence on extreme rainfall. This result is consistent with Kawamura et al. (2001) and Jin et al. (2005), which found strong rainfall over Fukuoka after strong La Niña events.

670 Following the idea of such stacking effects, an El Niño transitioning into a La Niña, if combined with the positive (Niño-like) phase of the PDV, would stack the strengthening influence of extreme rainfall over southern Kyushu. Both such cases would be exacerbated by the influence of the Trend+ mode. However, these are only hypotheses based on this study's statistical analysis, and the possibility of extreme rainfall probably does not stack linearly. Such scenarios should be investigated through sensitivity tests using numerical weather prediction models.

675 Recently, large ensemble climate prediction datasets such as d4PDF have been widely used in order to extract probabilities of occurrence of extreme weather such as tropical cyclones and heavy rainfalls. Attributing of such extreme events to global warming has been one of the foci in climate and impact assessment studies. In identifying the relationship of extreme events with specific climate modes, special care in evaluating the representation and performance of climate prediction datasets is 680 desirable. This study demonstrates one of the approaches for such evaluations.

Code availability

All software used to process the data are publicly available from their respective project webpages.

Data availability

685 Radar-AMeDAS may be ordered from JMA as CDROM catalogues. Rainfall from meteorological stations data may be downloaded from the JMA website at https://www.data.jma.go.jp/gmd/risk/obsdl/index.php. COBE-SST may downloaded from https://ds.data.jma.go.jp/tcc/tcc/products/elnino/cobesst/cobe-sst.html. The d4PDF data may be downloaded from https://diasjp.net/en/service/d4pdf-data-download.

Author contribution

690 Conceptualisation and Writing: Lee and Takemi. Investigation: Lee. Supervision and Project administration: Takemi.

Competing interests

The authors declare that they have no conflict of interest.

Acknowledgements

References

Alexander, M. A., Bladé, I., Newman, M., Lanzante, J. R., Lau, N. C., and Scott, J. D.: The atmospheric bridge: The influence of ENSO teleconnections on air–sea interaction over the global oceans. *J. Clim.*, **15(16)**, 2205-2231,
700 https://doi.org/10.1175/1520-0442(2002)015<2205:TABTIO>2.0.CO;2, 2002.

Bolton, D.: The computation of equivalent potential temperature. *Mon. Wea. Rev.*, **108(7)**, 1046-1053, https://doi.org/10.1175/1520-0493(1980)108<1046:TCOEPT>2.0.CO;2, 1980.

Campello, R. J. G. B., Moulavi, D., Sander, J.: Density-Based Clustering Based on Hierarchical Density Estimates, in: Advances in Knowledge Discovery and Data Mining. PAKDD 2013. Lecture Notes in Computer Science, vol 7819, edited
705 by Pei, J., Tseng, V.S., Cao, L., Motoda, H., Xu, G., Springer, Berlin, Heidelberg, Germany, 160–172. https://doi.org/10.1007/978-3-642-37456-2_14, 2013.

Met Office: Cartopy: a cartographic python library with a Matplotlib interface, https://scitools.org.uk/cartopy, 2010 – 2015.

Fujibe, F.: Annual variation of extreme precipitation intensity in Japan: Assessment of the validity of Clausius-Clapeyron scaling in seasonal change. *SOLA*, **12**, 106-10, https://doi.org/10.2151/sola.2016-024, 2016.

710 Guan, B. and Nigam, S.: Pacific sea surface temperatures in the twentieth century: An evolution-centric analysis of variability and trend. *J. Clim.*, **21(12)**, 2790-809, https://doi.org/10.1175/2007JCLI2076.1, 2008.

Harada, Y., Endo, H., and Takemura, K.: Characteristics of large-scale atmospheric fields during heavy rainfall events in western Japan: Comparison with an extreme event in early July 2018. *J. Meteorol. Soc. Japan. Ser. II*, **98(6)**, 1207-29, https://doi.org/10.2151/jmsj.2020-062, 2020.

715 Harris, C. R., and Coauthors: Array programming with NumPy. *Nature*, **585**, 357–62, https://doi.org/10.1038/s41586-020-2649-2.

Hirahara, S., M. Ishii, and Y. Fukuda, 2014: Centennial-scale sea surface temperature analysis and its uncertainty. *J. Clim.*, **27**, 57–75, https://doi.org/10.1175/JCLI -D-12-00837.1, 2020.

Horel, J. D., and Wallace, J. M.: Planetary-scale atmospheric phenomena associated with the interannual variability of sea
720 surface temperature in the equatorial Pacific. *Mon. Wea. Rev.*, **109**, 813–829, https://doi.org/10.1175/1520-0493(1981)109<0813:PSAPAW>2.0.CO;2, 1981.

Hoskins, B. J., and Karoly, D. J.: The steady linear response of a spherical atmosphere to thermal and orographic forcing. *J. Atmos. Sci.*, **38**, 1179–1196, https://doi.org/10.1175/1520-0469(1981)038<1179:TSLROA>2.0.CO;2, 1981.

Hoyer, S. and Hamman, J.: xarray: N-D labeled Arrays and Datasets in Python. *Journal of Open Research Software*, **5(1)**, 10,
725 https://doi.org/10.5334/jors.148, 2017.

Hunter, J. D.: Matplotlib: A 2D graphics environment. *Computing in Science & Engineering*, **9(3)**, 90–5, https://doi.org/10.1109/MCSE.2007.55, 2007.

Ishii, M., Shouji, A., Sugimoto, S., and Matsumoto, T.: Objective Analyses of Sea-Surface Temperature and Marine Meteorological Variables for the 20th Century using ICOADS and the Kobe Collection. *Int. J. Climatol.*, **25**, 865-879,
730 https://doi.org/10.1002/joc.1169 , 2005.

Ishii M., and Mori, N.: d4PDF: large-ensemble and high-resolution climate simulations for global warming risk assessment. *Prog. Earth Planet Sci.*, **7(1)**, 1-22, https://doi.org/10.1186/s40645-020-00367-7, 2020.

Japan Meteorological Agency: Characteristics of Global Sea Surface Temperature Analysis Data (COBE-SST) for Climate Use. Monthly Report on Climate System Separated Volume, 12, 116pp, 2006.

735 Jin, Y. H., Kawamura, A., Jinno, K., and Berndtsson, R.: Quantitative relationship between SOI and observed precipitation in southern Korea and Japan by nonparametric approaches. *Journal of Hydrology*, **301(1-4)**, 54-65, https://doi.org/10.1016/j.jhydrol.2004.06.026, 2005.

Kamae, Y., Imada, Y., Kawase, H., and Mei, W.: Atmospheric rivers bring more frequent and intense extreme rainfall events over East Asia under global warming. *Geophys. Res. Lett.*, **48**, e2021GL096030, https://doi.org/10.1029/2021GL096030, 740   2021.

Kawamura, A., Eguchi, S., and Jinno, K.: Correlation between Southern Oscillation and monthly precipitation in Fukuoka. *Journal of Japan Society of Civil Engineers*, **2001(691)**, 153-8. https://doi.org/10.2208/jscej.2001.691_153, 2001.

Kawase, H., and CoAuthors: Identifying robust changes of extreme precipitation in Japan from large ensemble 5-km-grid regional experiments for 4K warming scenario. *J. Geophys. Res.-Atmos,* **128(18)**, https://doi.org/10.1029/2023JD038513, 745   2023.

Kobayashi, S., and CoAuthors: The JRA-55 reanalysis: General specifications and basic characteristics. *J. Meteorol. Soc. Japan. Ser. II*, **93(1)**, 5-48, https://doi.org/10.2151/jmsj.2015-001, 2015.

Kosaka, Y., Xie, S. P., Lau, N. C., and Vecchi, G. A.: Origin of seasonal predictability for summer climate over the Northwestern Pacific. *Proc. Natl. Acad. Sci. U.S.A.*, **110(19)**, 7574-9, https://doi.org/10.1073/pnas.1215582110, 2013.

750   Knapp, K. R., Diamond, H. J., Kossin, J. P., Kruk, M. C., and Schreck, C. J.: International Best Track Archive for Climate Stewardship (IBTrACS) Project, Version 4. NOAA National Centers for Environmental Information, https://doi.org/10.25921/82ty-9e16, 2018.

Lee, S., L'Heureux, M., Wittenberg, A. T., Seager, R., O'Gorman, P. A., and Johnson, N. C.: On the future zonal contrasts of equatorial Pacific climate: Perspectives from Observations, Simulations, and Theories. *npj Clim. Atmos. Sci.*, **5**, 82, 755   https://doi.org/10.1038/s41612-022-00301-2, 2022.

Li, Y., Deng, Y., Yang, S., and Zhang, H.: Multi-scale temporospatial variability of the East Asian Meiyu-Baiu fronts: characterization with a suite of new objective indices. *Clim Dyn*, **51**, 1659–1670, https://doi.org/10.1007/s00382-017-3975-4, 2018.

Matsumoto, S., Ninomiya, K., and Yoshizumi, S.: Characteristic features of "Baiu" front associated with heavy rainfall. *J.* 760   *Meteorol. Soc. Japan. Ser. II*, **49(4)**, 267-281, https://doi.org/10.2151/jmsj1965.49.4_267, 1971.

McKinney W.: Data structures for statistical computing in python, in Proceedings of the 9th Python in Science Conference. p. 51–6. https://doi.org/10.25080/Majora-92bf1922-00a, 2010.

Mizuta, R., and Coauthors: Over 5,000 years of ensemble future climate simulations by 60-km global and 20-km regional atmospheric models. *Bull. Amer. Meteor. Soc.*, **98(7)**,1383-98, https://doi.org/10.1175/BAMS-D-16-0099.1, 2017.

765   Mizuta, R., and Coauthors: Climate simulations using MRI-AGCM3.2 with 20-km grid. *J. Meteorol. Soc. Japan. Ser II*, **90**, 233–258, https://doi.org/10.2151/jmsj.2012- A12, 2012.

Mori, N., and Takemi, T.: Impact assessment of coastal hazards due to future changes of tropical cyclones in the North Pacific Ocean. *Weather and Climate Extremes*, **11**, 53-69, https://doi.org/10.1016/j.wace.2015.09.002, 2016.

Mori, N., and Coauthors: Recent nationwide climate change impact assessments of natural hazards in Japan and East Asia. 770   *Weather and Climate Extremes*, **32**, 100309, https://doi.org/10.1016/j.wace.2021.100309, 2021.

Nagata, K.: Quantitative precipitation estimation and quantitative precipitation forecasting by the Japan Meteorological Agency. *RSMC Tokyo–Typhoon Center Technical Review*, **13**, 37-50, 2011. (Available online at: http://www.jma.go.jp/jma/ jma-eng/jma-center/rsmc-hp-pub-eg/techrev/text13-2.pdf)

Naka, N., and Takemi, T.: Characteristics of the environmental conditions for the occurrence of recent extreme rainfall 775   events in northern Kyushu, Japan. *Sci. Online Lett. Atmos.*, **19A**, 9-16, https://doi:10.2151/sola.19A-002, 2023.

Naoi, M., Kamae, Y., Ueda, H., and Mei, W.: Impacts of seasonal transitions of ENSO on atmospheric river activity over East Asia. *J. Meteor. Soc. Japan*, **98**, 655–668, https://doi.org/10.2151/jmsj.2020-027, 2020.

Nayak, S., and Takemi, T.: Dependence of extreme precipitable water events on temperature. *Atmósfera*, **32(2)**, 159-65, https://doi.org/10.20937/atm.2019.32.02.06, 2019.

780   Nayak, S., and Takemi, T.: Atmospheric driving mechanisms of extreme precipitation events in July of 2017 and 2018 in western Japan. *Dynamics of Atmospheres and Oceans*, **93**, 101186, https://doi.org/10.1016/j.dynatmoce.2020.101186, 2021.

The NCAR Command Language (Version 6.6.2) [Software]. Boulder, Colorado: UCAR/NCAR/CISL/TDD. https://doi.org/10.5065/D6WD3XH5, 2019.

Ninomiya K., and Mizuno, H.: Variations of Baiu precipitation over Japan in 1951-1980 and large-scale characteristics of 785   wet and dry Baiu. *J. Meteorol. Soc. Japan. Ser. II*, 1987, **65(1)**, 115-27, https://doi.org/10.2151/jmsj1965.65.1_115, 1987.

Nitta, T.: Convective activities in the tropical western Pacific and their impact on the Northern Hemisphere summer circulation. *J. Meteorol. Soc. Japan. Ser. II*, **65(3)**, 373-90, https://doi.org/10.2151/jmsj1965.65.3_373, 1987.

Ohba, M., Kadokura, S., Yoshida, Y., Nohara, D., and Toyoda, Y.: Anomalous weather patterns in relation to heavy precipitation events in Japan during the Baiu season. *J. Hydrometeorol*, **16(2)**, 688-701, https://doi.org/10.1175/JHM-D-14-0124.1, 2015.

Sakashita, W., Yokoyama, Y., Miyahara, H., Yamaguchi, Y. T., Aze, T., Obrochta, S. P., and Nakatsuka, T.: Relationship between early summer precipitation in Japan and the El Niño-Southern and Pacific Decadal Oscillations over the past 400 years. *Quaternary International*, **397**, 300-6, https://doi.org/10.1016/j.quaint.2015.05.054, 2016.

Sasaki, H., Murata, A., Hanafusa, M., Oh'izumi, M., and Kurihara, K.: Reproducibility of present climate in a non-hydrostatic regional climate model nested within an atmosphere general circulation model. *SOLA*, **7**, 173–176, https://doi.org/10.2151/sola.2011-044, 2011.

Schulzweida, U.: CDO User Guide (2.1.0). Zenodo [code], https://doi.org/10.5281/zenodo.7112925, 2022.

Takaya, Y., Ishikawa, I., Kobayashi, C., Endo, H., and Ose, T.: Enhanced Meiyu-Baiu rainfall in early summer 2020: Aftermath of the 2019 super IOD event. *Geophys. Res. Lett.*, **47**, e2020GL090671, https://doi.org/10.1029/2020GL090671, 2020.

Takemura, K., Mukougawa, H., and Maeda, S.: large-scale atmospheric circulation related to frequent rossby wave breaking near Japan in boreal summer. *J. Clim.*, **33(15)**, 6731-44, https://doi.org/10.1175/JCLI-D-19-0958.1, 2020.

Takemura, K., Mukougawa, H.: A new perspective of Pacific–Japan pattern: Estimated percentage of the cases triggered by Rossby wave breaking. *J. Meteorol. Soc. Japan. Ser. II*, **100(1)**, 115-39, https://doi.org/10.2151/jmsj.2022-006, 2022.

Tanaka, M.: Interannual and interdecadal variations of the western North Pacific monsoon and Baiu rainfall and their relationship to the ENSO cycles. *J. Meteorol. Soc. Japan. Ser. II*, **75(6)**, 1109-23, https://doi.org/10.2151/jmsj1965.75.6_1109, 1997.

Unuma, T., and Takemi, T.: Rainfall characteristics and their environmental conditions during the heavy rainfall events over Japan in July of 2017 and 2018. *J. Meteorol. Soc. Japan. Ser. II*, **99(1)**, 165-80, https://doi.org/10.2151/jmsj.2021-009, 2021.

Vecchi, G. A., Clement, A., and Soden, B. J.: Examining the tropical Pacific's response to global warming. *Eos, Transactions American Geophysical Union*, **89(9)**, 81-3, https://doi.org/10.1029/2008EO090002, 2008.

Virtanen, P., and Coauthors: SciPy 1.0: Fundamental Algorithms for Scientific Computing in Python. *Nature Methods*, **17**, 261–72, https://doi.org/10.1038/s41592-019-0686-2, 2020.

Wang, B., Wu, R., and Fu, X.: Pacific–East Asian teleconnection: how does ENSO affect East Asian climate?. *J. Clim.*, **13(9)**, 1517-36, https://doi.org/10.1175/1520-0442(2000)013<1517:PEATHD>2.0.CO;2, 2000.

Webb, A., Shimura, T., and Mori, N.: Global tropical cyclone track detection and analysis of the d4PDF mega-ensemble projection. *Journal of Japan Society of Civil Engineers, Ser. B2 (Coastal Engineering)*, 75(2), I_1207-12, https://doi.org/10.2208/kaigan.75.I_1207, 2019.

Weare, B. C., and Nasstrom, J. S.: Examples of extended empirical orthogonal function analyses. *Mon. Wea. Rev.*, **110(6)**, 481-5, https://doi.org/10.1175/1520-0493(1982)110<0481:EOEEOF>2.0.CO;2, 1982.

Xie, S. P., Kosaka, Y., Du, Y., Hu, K., Chowdary, J. S., and Huang, G.: Indo-western Pacific Ocean capacitor and coherent climate anomalies in post-ENSO summer: A review. *Adv. Atmos. Sci.*, **33(4)**, 411-32, https://doi.org/10.1007/s00376-015-5192-6, 2016.

Yokoyama, C., Tsuji, H., and Takayabu, Y. N.: The effects of an upper-tropospheric trough on the heavy rainfall event in July 2018 over Japan. *J. Meteorol. Soc. Japan. Ser. II*, **98(1)**, 235-55, https://doi.org/10.2151/jmsj.2020-013, 2020.

Zhang, W., Huang, Z., Jiang, F., Stuecker, M. F., Chen, G., and Jin, F.-F.: Exceptionally persistent Madden-Julian Oscillation activity contributes to the extreme 2020 East Asian summer monsoon rainfall. *Geophys. Res. Lett.*, **48**, e2020GL091588, https://doi.org/10.1029/2020GL091588, 2021.